Polymer 50 (2009) 3714–3723

Contents lists available at ScienceDirect

Polymer

journal homepage: www.elsevier.com/locate/polymer

Plastic deformation of spherulitic semi-crystalline polymers: An *in situ* AFM study of polybutene under tensile drawing

C. Thomas, R. Seguela*, F. Detrez [1], V. Miri, C. Vanmansart

Laboratoire Structure et Propriétés de l'Etat Solide, Université de Lille1 – CNRS, 59655 Villeneuve d'Ascq, France

ARTICLE INFO

Article history:
Received 4 June 2009
Accepted 8 June 2009
Available online 16 June 2009

Keywords:
Polybutene
Atomic force microscopy
Spherulites

ABSTRACT

The plastic deformation of semi-crystalline polybutene (PB) has been studied at the micrometric and nanometric scales by Atomic Force Microscopy (AFM). Owing to a movable tensile drawing stage, capturing images from the same locus of the sample allowed for quasi *in situ* observations of the plastic processes. In the case of PB films having an average spherulite diameter of about 20 μm, the macroscopic deformation was homogeneous over the whole gauge length of the sample, up to rupture. In parallel, the local deformation at the scale of the spherulites was very close to homogeneous and obeyed an affine deformation law over the whole strain range: the shape of the deformed spherulites was kept roughly elliptical up to rupture without clues of fibrillar transformation. The inter-spherulitic boundaries displayed very high cohesion. Fragmentation of the crystalline lamellae proved to be a predominant process, while crystal slip could not be detected at the scale of the AFM resolution, i.e. a few nanometers. Wide-angle and small-angle X-ray scattering yet revealed the occurrence of crystal plastic shear. Similar observations have been made in the case of PB films having an average spherulite diameter of about 5 μm. In the conclusion, a comparison is made with a previous study regarding the deformation mechanisms of a PB sample having 200 μm wide spherulites which displayed brittle behavior.

1. Introduction

In recent years, the demand for predictive approaches of the mechanical behavior of semi-crystalline polymers has aroused increasing efforts for introducing physical concepts in the mechanical modeling (see Ref. [1] and refs cited therein). Benefiting from the drastic increase of computing capacities, this resulted in the development of complex strategies that can yet only account for a limited number of factors of the structural hierarchy of semi-crystalline polymers. Moreover, the deformation processes at the various scale levels of the structure are far for being thoroughly understood, so that numerous assumptions have to be used in the modeling.

Poly(1-butene), otherwise PB, is a kind of "model system" for studying the incidence of the various structural factors on the mechanical behavior, keeping constant the physico-chemistry and the crystallography of the system. Indeed, the morphological habits of PB are strongly sensitive to the crystallization conditions [2]. The spherulite size can be as large as 500 μm down to 3 μm, the crystallinity being in the range 60–40%. The crystal thickness, in the range 20–8 nm, is particularly convenient for performing investigations by Atomic Force Microscopy (AFM). We recently reported [3] the quasi *in situ* AFM study of the plastic deformation mechanisms of PB films having large spherulites of diameter 200 ± 20 μm. Owing to the isothermal crystallization of the films from the melt with a free surface, a good number of adjacent spherulites could grow with their core located right on the free surface of the film. This made it possible capturing the plastic deformation processes at a nanometric scale within the various regions of the spherulites, without any chemical treatment. Under tensile drawing, crazing appeared to be the predominant process of plastic deformation in the equatorial regions, whereas profuse lamella fragmentation developed in the polar regions. Combinations of the two processes occurred in the diagonal regions. The material broke in a relatively brittle manner at a strain of about 15%.

In the present paper, we address the plastic behavior of PB films having small size spherulites, i.e. below 20 μm in diameter. Such films display much greater ductility than the ones of the former study. Besides, considering that the film thickness (about 100 μm) is much greater than the spherulite size, we can easily assume that the AFM surface observations of the deformation processes are representative of the bulk-operating processes that emerge at the sample surface. This point was already argued in the previous work

* Corresponding author. Tel.: +33 3 20 43 47 80; fax: +33 3 20 43 65 91.
E-mail address: roland.seguela@univ-lille1.fr (R. Seguela).
[1] Present address: Mines Paristech, Centre des Materiaux, 91003 Evry, France.

0032-3861/$ – see front matter © 2009 Elsevier Ltd. All rights reserved.
doi:10.1016/j.polymer.2009.06.023

[3] from experimental findings that gave evidence of stress triaxiality. We will point out some particular features of the deformation processes that must be ascribed to free surface effects but do not modify the general conclusions.

2. Experimental

The poly(1-butene) material (PB) from Shell has number- and weight-average molar weights $M_n \approx 28$ kDa and $M_w \approx 174$ kDa. The polymer pellets were compression-molded into 100 μm thick sheets between steel plates at 170 °C for 2 min before cooling at about 20°/min. Borrowing from Weynant's isothermal crystallization study [2], two kinds of polymer films were prepared: the initial sheets were melted again at 170 °C on a steel plate with free-upper surface for 5 min, before to be quenched into a water bath at either 25 °C and 0 °C. The films were stored for at least 5 days at room temperature (RT) prior to investigation in order to promote complete structural transformation of the thermodynamically unstable tetragonal crystals grown during the crystallization step into the stable hexagonal crystal form [2,4,5].

After structural stabilization, the average spherulite size determined from AFM experiments (see details below) was 20 ± 5 μm (PB-20) and 5 ± 2 μm (PB-5) for the crystallization at 25 °C and 0 °C, respectively. The peak temperature and crystallinity were determined by Differential Scanning Calorimetry (DSC) using a DSC-7 calorimeter (Perkin–Elmer, Waltham MA, USA) at a heating rate of 10°/min. The crystal weight fraction, X_c, was computed from the melting enthalpy of the samples as compared with the melting enthalpy of perfectly crystalline PB, i.e. $\Delta H_f = 120$ J/g [6].

The glass transition of the amorphous phase not observable from the DSC trace was determined by Dynamic Mechanical Analysis using an RSA3 apparatus (TA Instruments, Wilmington DE, USA) at 1 Hz and a heating rate of 1 °C/min.

Wide-Angle X-ray Scattering (WAXS) and Small-Angle X-ray Scattering (SAXS) experiments have been performed in transmission mode using the Ni-filtered Kα radiation of a 2kW sealed tube (Panalytical, Paris, France). The 2D-patterns were recorded on a CCD camera (Photonic Science, Millham, UK) placed at 50 mm and 800 mm from the sample for WAXS and SAXS, respectively.

Atomic Force Microscopy observations were performed at RT on a Dimension 3100 apparatus (Digital Instruments, Santa Barbara, USA) operated in Tapping mode™. The Nanoworld silicon SPM sensors (type NCL) had a tip radius less than 10 nm, the nominal spring constant and resonance frequency of the cantilever being respectively 48 Nm^{-1} and 190 kHz. The *height* and *error* images were recorded in a so-called light tapping mode using a set-point amplitude ratio $r_{sp} \approx 0.9$–0.95 that prevents indentation in order to optimize the topographic contrast. This point is largely discussed in Ref. [7]. The 512×512 pixels images were recorded by operating the 90×90 mm^2 piezoelectric scanner at a scanning rate of 0.5 Hz. The *error* images, often abusively referred to as *amplitude* images, are displayed to enhance the visibility of the topological features by highlighting the regions of large variations of the AFM cantilever oscillations. The AFM apparatus was equipped with a home-made drawing stage that enabled stepwise deformation of films at constant crosshead speed and holding the sample at chosen constant strains for the duration of the image recording [3]. The initial strain rate was 10^{-3} s^{-1} and the samples were allowed to relax for 10 min before starting image recording for several tens of minutes at practically constant stress. The whole microscope was enclosed in a coffer for preventing vibrations during the image recordings. The macroscopic or engineering tensile strain, $\varepsilon = \Delta L/L_o$, was determined from the displacement of the crosshead ΔL, L_o being the sample gauge length. The local strain, ε_{local}, at the scale of the spherulites was occasionally estimated from the AFM images using the displacement of specific details at the centre of the spherulites and about the inter-spherulitic boundaries. All AFM images are reported with the tensile direction oriented vertical.

Table 1
Structural parameters of the PB films.

Material	Spherulite diameter (μm)	Crystallinity (weight %)	Melting point (°C)	Crystal thickness (nm)
PB-5	5 ± 2	44 ± 1	119.5 ± 0.5	8 ± 2
PB-20	20 ± 5	49 ± 1	120.5 ± 0.5	10 ± 2
PB-200	200 ± 50	55 ± 1	123.5 ± 0.5	15 ± 2

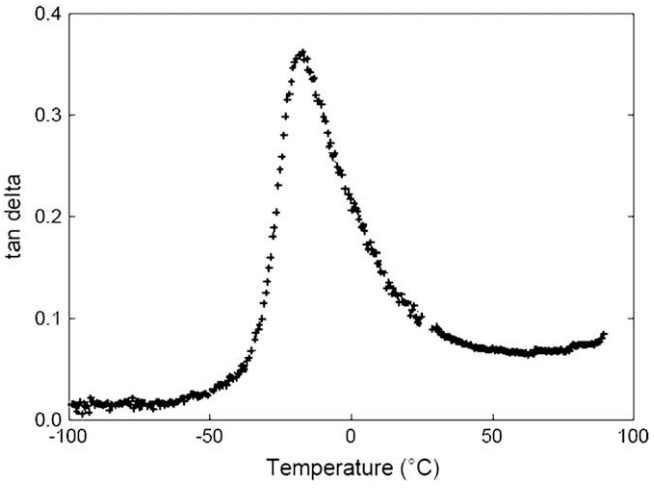

Fig. 1. Loss tangent versus temperature for PB-20.

3. Results

The structural and physical characteristics of the PB-20 and PB-5 films are reported in Table 1. The crystalline lamella thickness was estimated from the long period of the lamellar stacking determined from AFM *height* images and the DSC crystal volume fraction, taking the densities $\rho_c = 0.95$ g/cm^3 and $\rho_a = 0.87$ g/cm^3 for the crystalline and the amorphous phase, respectively [8]. In spite of quite large departure in spherulite diameter, the two kinds of films have very close crystallinity and crystal thickness, and melting point as well.

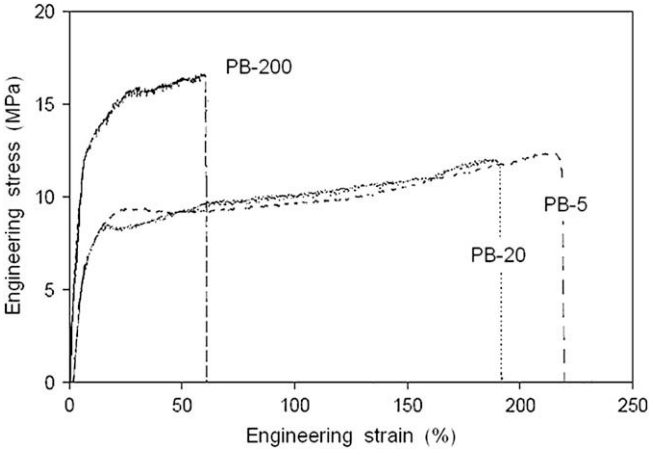

Fig. 2. Engineering stress–strain curves of the PB-20 and PB-5 films at room temperature, for an initial strain rate of 10^{-3} s^{-1} (the data for PB-200 are included for comparison).

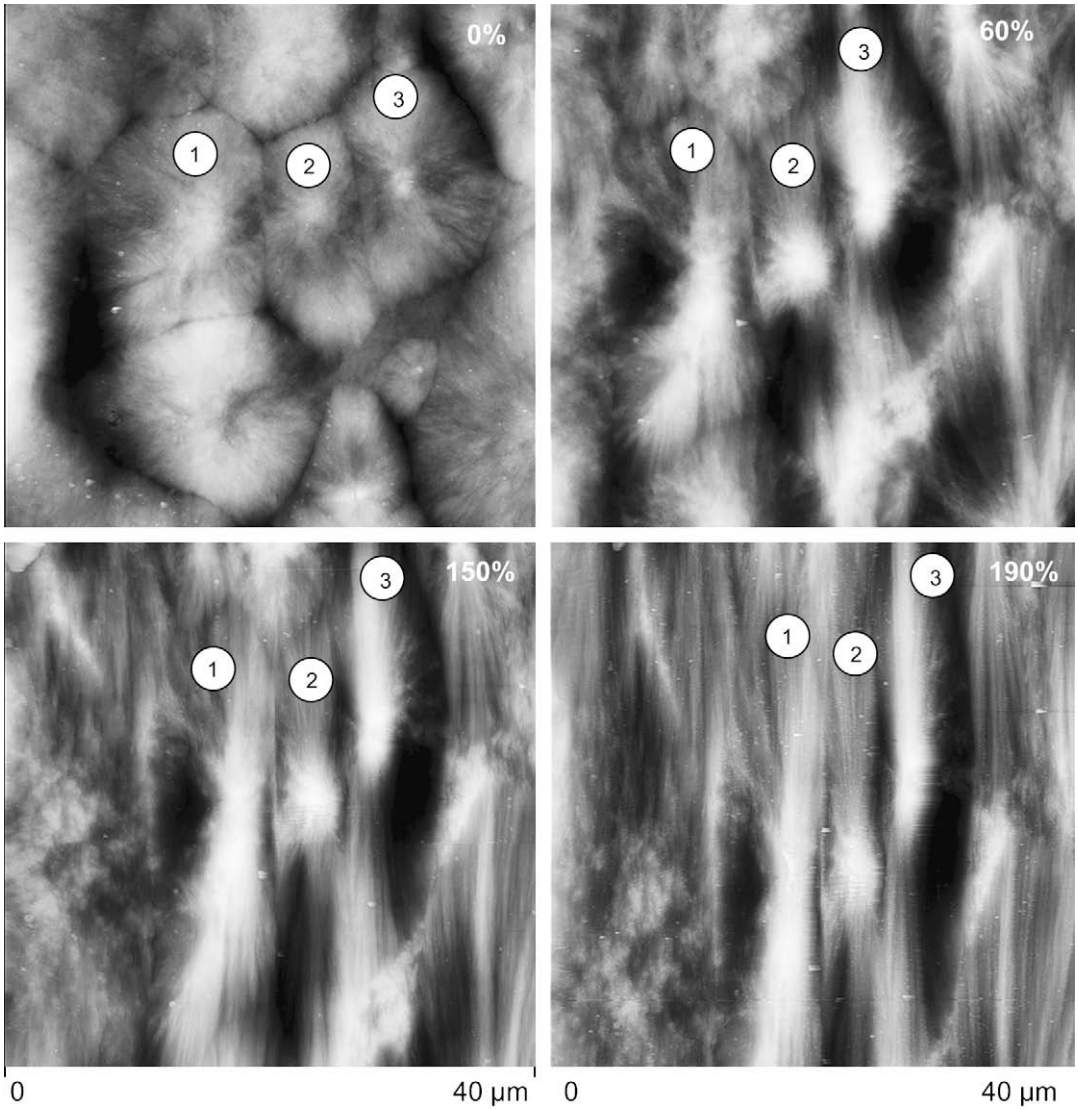

Fig. 3. Large scale AFM *height* images ($Z_{range} = 3200$ nm) of PB-20 for strains $\varepsilon = 0\%$, $\varepsilon = 60\%$, $\varepsilon = 150\%$ and $\varepsilon = 190\%$.

For the sake of comparison, Table 1 also includes structural data for the PB film of average spherulite diameter 200 ± 50 μm (PB-200) concerned with the previous paper [3]. For this film obtained by isothermal crystallization for 2 h at 80 °C, both the melting point and crystal thickness are somewhat greater than those of the PB-20 and PB-5.

The loss tangent data reported in Fig. 1 show a main relaxation peak at about −20 °C, indicating that the amorphous phase is rubbery at RT, i.e. the temperature of the AFM experiments.

Fig. 2 shows the engineering stress–strain curves of PB-20 and PB-5 samples under monotonic tensile drawing. Both materials display extremely faint stress drop at the yield point, if any, and a rather steady strain-hardening beyond. This is related to a homogeneous plastic deformation at the macroscopic scale that is actually observed from the uniform reduction of the sample width with increasing strain. The large strain at break contrasts with the brittle behavior of the previously studied PB-200.

3.1. PB-20 films

Fig. 3 shows large scale *height* images of PB-20 embracing several spherulites as a function of strain. Close examination reveals that the spherulite deformation is fairly homogeneous and affine to the macroscopic deformation up to $\varepsilon = 190\%$, i.e. close to rupture. For instance, for $\varepsilon = 60\%$, the local strain is $\varepsilon_{local} = 55 \pm 5\%$ for the spherulites labeled #1, #2 and #3; for $\varepsilon = 190\%$, the local strain of spherulites #1 and #2 is $\varepsilon_{local} = 200 \pm 20\%$. No craze can be seen at the same scale at which intense crazing was clearly observed in the previous study of PB films with 200 μm spherulites [3]. In spite of the high strain level, the spherulite structure is preserved up to rupture without hints of fibrillar transformation. These observations suggests that the uniform plastic deformation at the macroscopic scale, i.e. without necking, results from a homogeneous activation of plastic processes at the local scale of the spherulites. The absence of crazing, that is a typically unstable process, is a major feature of the PB-20 mechanical behavior.

It is worth noticing that the core and polar regions of the deformed spherulites appear at higher elevation than the equatorial regions as can be seen from the brightness of these regions in the *height* images of Fig. 3. The *error* images of Fig. 4 provide closer view and better resolution of the topological details of the deformed spherulites #2 and #3 from Fig. 3 at the strains 0% and 60%. This observation means that the core and polar regions of the spherulites have been slightly pushed up above the average

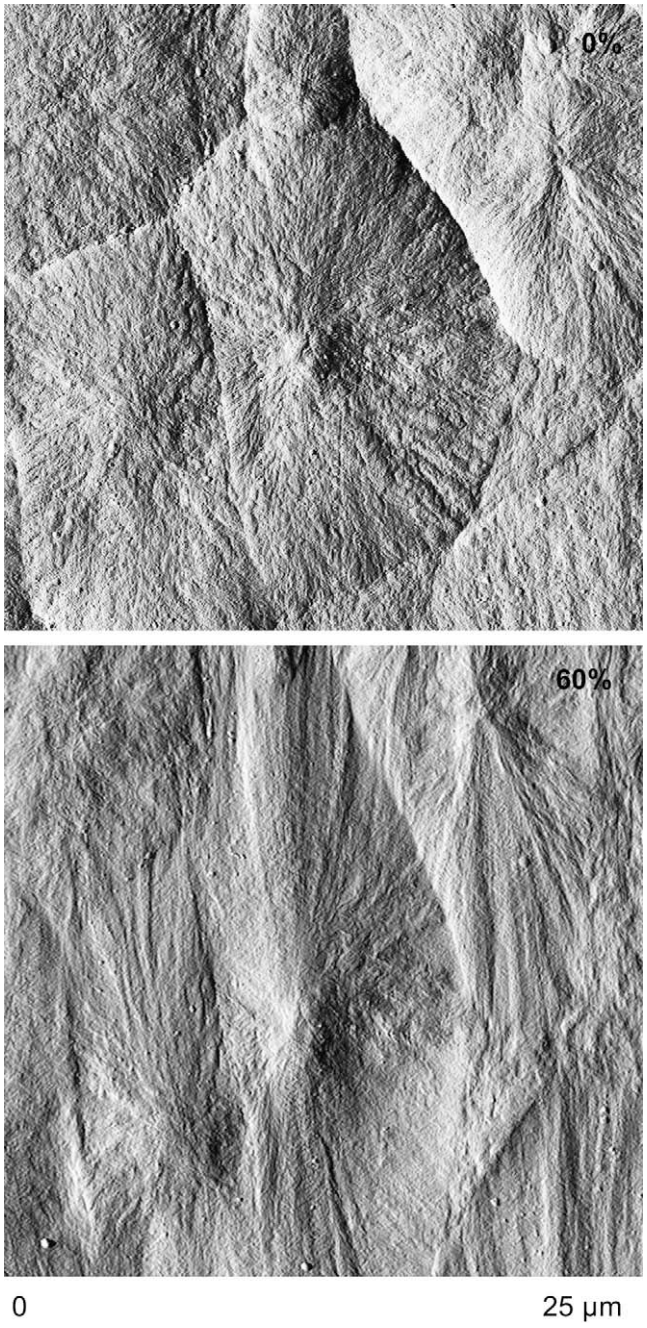

Fig. 4. Medium scale AFM *error* images of PB-20 for the strains $\varepsilon = 0\%$ and $\varepsilon = 60\%$ (the central spherulites are the ones labeled #2 and #3 in Fig. 3).

level of the sample surface as a result of the plastic deformation. This gives indication that the bulk plastic deformation processes coming from inside the film do not strictly display the same activity in the various regions of the spherulites. The plastic strain heterogeneity in these various regions is yet rather faint in consideration that the maximum surface roughness of 3200 nm (see the Z_{range} of Fig. 3) is small with regard to both the spherulite size and film thickness. This suggests that the plastic processes are not much disturbed when emerging at the free film surface, so that surface observations are fairly representative of the bulk phenomena.

A second point that is worth noticing from Fig. 4 is the strong cohesiveness of the material at the inter-spherulitic boundaries as revealed by the absence of cavitation or damage processes, at least at the scale level of the AFM resolution, i.e. a few nanometers. This observation is relevant to an efficient transmission of the stress between adjacent spherulites that is a prime role factor for the affine deformation at the scale of the spherulites. In addition, the topological singularity of the boundaries becomes less distinct with increasing plastic strain, and even almost disappears in some places. This observation corroborates the previous conclusion that bulk deformation prevails over surface effects: indeed, if the latter ones were dominant, boundary topological features would turn more pronounced.

Fig. 5 provides more precise analysis of the polar, diagonal and equatorial regions of the deformed spherulite #3 of Fig. 4. The small scale *error* images disclose an intense fragmentation of the crystalline lamellae without noticeable cavitation between the fragments. The fragmentation process looks quite uniform over the whole spherulite volume since the lamella fragments have a fairly narrow size distribution with an average size of about 20 nm. This figure is surprisingly close to the stacking long period of PB-20. A similar observation was previously reported by Ferreiro et al. [7] regarding the *ex situ* AFM study of the plastic deformation of nylon6. It was suggested that the activation of interlamellar slip in some lamellar stacks having favorable oblique orientation for shear could cross the neighbor lamellar stacks of opposite orientation and thus promote intralamellar crystal slip. This kind of phenomenon is likely to leave the footprint of the stacking long period on the remaining fragments.

Another worth noticing feature in Fig. 5 is the rather regular alignment of the crystal fragments along oblique lines at $\beta \approx 50^\circ$ from the tensile direction (see the white doted lines on the images of Fig. 5). This is a typical feature of plastic shear in polymers that occurs at $\beta > 45^\circ$ under tensile test owing to the well-known piezo-dependence, an inherent property of polymers due to their low packing density. According to the yielding Coulomb criteria [9], plastic shear proceeds when the applied shear stress, τ, obeys

$$\tau > \tau^\circ - \mu\sigma_n \tag{1}$$

where τ° is the critical resolved shear stress, σ_n is the normal stress on the shear plane, $\mu = \cot 2\theta$ is the friction coefficient, and θ is the angle between the normal to the shear plane and the main tensile stress. Then, considering a typical value $0.1 < \mu < 0.2$ for most semi-crystalline and glassy polymers [10], it turns out that $39^\circ < \theta < 42^\circ$, and the tilt angle of the shear plane with respect to the tensile testing direction should be $48 < \beta < 51^\circ$.

Homogeneous or uniform crystal slip generally takes place in concert with heterogeneous or localized crystal slip [11,12] during the plastic deformation of polyolefin-based polymers, and more generally in semi-crystalline polymers. In the present case, the intense lamella fragmentation suggests predominant activation of localized crystal slip. More accurate examination of the fragmentation process can be made from Fig. 6 which reports both *height* and *error* images, at the same scale as in Fig. 5, for samples deformed at lower strains, i.e. just beyond the yield point. These images reveal that fragmentation takes place sporadically giving rise to crystal fragments of highly distributed sizes. Increasing strain promotes a gradual breaking of the larger lamellar fragments into smaller ones, reducing the broadness of the block size distribution. It should also be noticed that fragmentation first proceeds in the spherulite core region and gradually invades the periphery with increasing strain. This means that some plastic strain gradient exists along the radius of the spherulites in the former stages of plastic deformation. The growth of the radial lamellae from the crystalline nucleus at the core of the spherulites

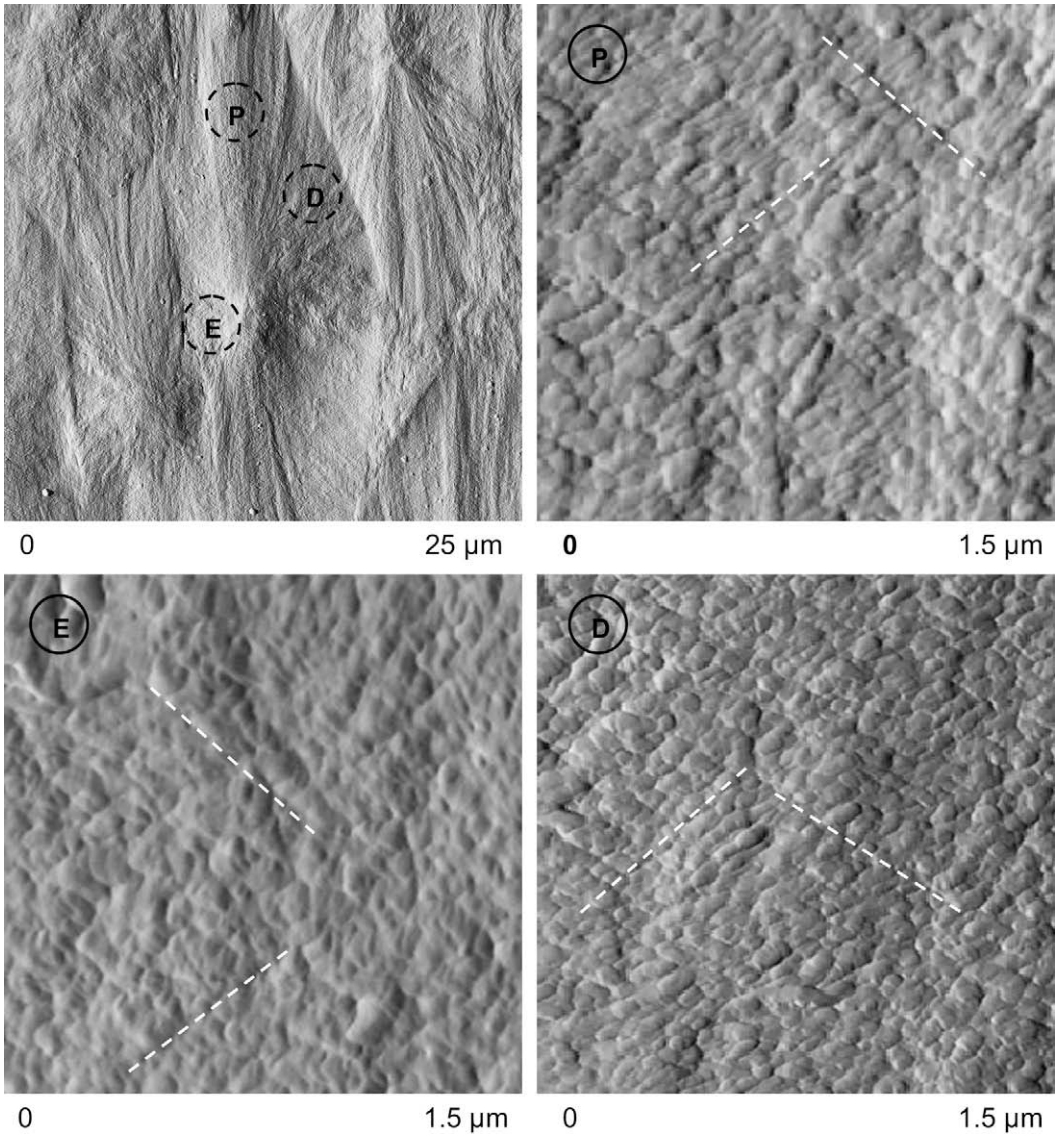

Fig. 5. Small scale AFM *error* images of PB-20 drawn at $\varepsilon = 60\%$ from the equatorial (E), polar (P) and diagonal (D) regions of spherulite #3 from Fig. 4.

involves a higher local stiffness than the average value which makes this region more prone to brittle processes. Away from the core, the rubbery amorphous matrix embedding the crystalline lamellae is able to accommodate a part of the applied deformation via visco-elasticity and thus delay plasticity and fragmentation processes. To finish with, the small scale images of Fig. 6 corroborate the absence of fibrillar transformation pointed out above.

In the present instance, the sporadic occurrence of fragmentation supports a self-governed process ruled out by a critical stress criterion for crystal slip or cleavage. However, the homogenization of the crystal block size at large strains together with the oblique alignment of the fragments suggests that the fragmentation process may benefit from the activation of large scale slip, including interlamellar slip, in agreement with Ferreiro et al. [7].

The *height* images of Fig. 6 offer a better opportunity than the *error* images for checking the occurrence of cavitation owing to the Z_{range} data. For the sake of comparison, Fig. 7 shows a *height* image at the same scale and at about the same strain for the PB film having 200 μm spherulites that displayed brittle behavior. The dark regions in the cracks and crazes indicate that the sample roughness spans the whole $Z_{range} = 2500$ nm. This *height* value that is much greater than the lamella thickness of PB-200 is relevant to actual cavitation in the darker regions of Fig. 7. The maximum roughness of PB-20 is much less than that of PB-200 since the *height* images of Fig. 6 at the same scale have only a $Z_{range} = 120$ nm. This does not mean that cavitation is completely absent in sample PB-20 but that it is largely less than in PB-200.

Fig. 8 exhibits a small scale *error* image of PB-20 for the strain $\varepsilon = 150\%$. Crystal fragments are still observable with a preferred oblique orientation. This orientation is yet closer to the draw axis than for $\varepsilon = 60\%$: the average tilt angle of the block alignments at about 40° means that the fragments have rotated towards the draw axis with increasing strain, without significant change of block size that is still about 20 nm. There is still no hint of fibrillar transformation.

The SAXS and WAXS patterns of PB-20 drawn at $\varepsilon = 150\%$ are shown in Fig. 9. The 4-point SAXS pattern (Fig. 9a) is relevant to a highly textured semi-crystalline material with lamellar scattering elements having their normal tilted at roughly 50° to the

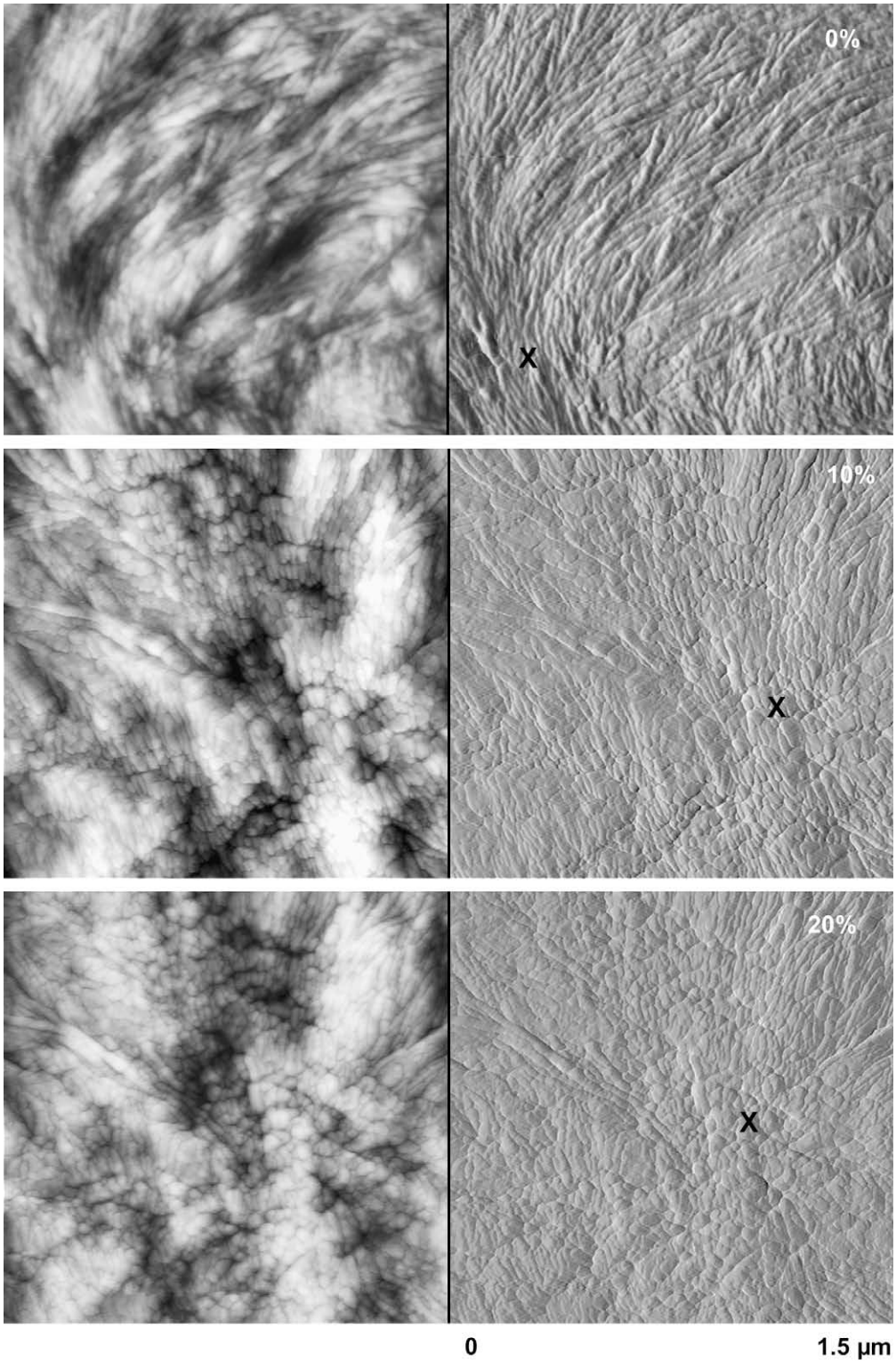

Fig. 6. Small scale AFM *height* images (left column; $Z_{range} = 120$ nm) and *error* images (right column) of PB-20 at various low strains in the range $0 < \varepsilon < 20\%$ (the *X* indicates the locus of the spherulite core in every image).

draw axis. This means that the lamellae surface is inclined at about 40° from the draw axis, in perfect consistency with the AFM image of Fig. 8. The orientation of the SAXS lobes with respect to the scattering vector (Fig. 9a) indicates that the axis of the lamella stacks is oblique to the draw direction and could be ascribed to a rigid rotation of the stacks, with little shear if any [13,14]. Such situation is quite infrequent in the case of semi-crystalline polymers [15]. However, it has been clearly identified in the case of deformation of lamellar triblock copolymers with rubbery midblock and stiff endblocks that are structural homologs

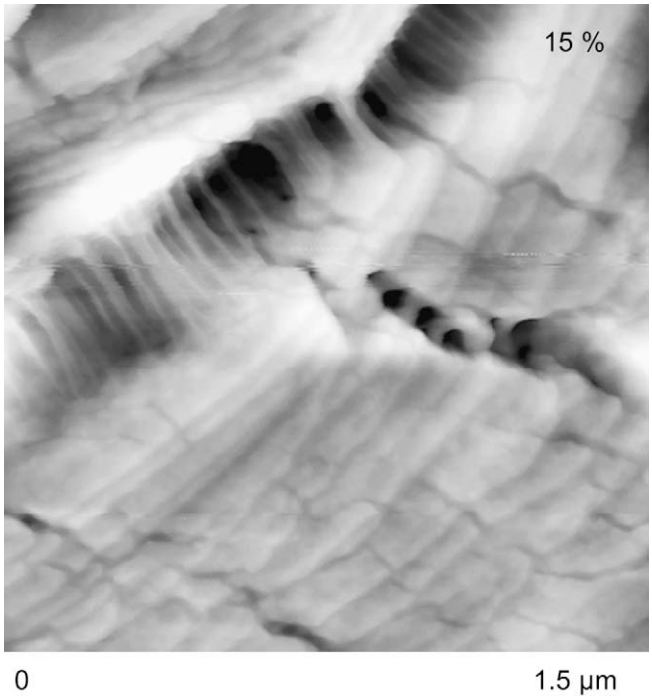

Fig. 7. Small scale AFM *height* image ($Z_{range} = 2500$ nm) of PB-200 at the strain $\varepsilon = 15\%$.

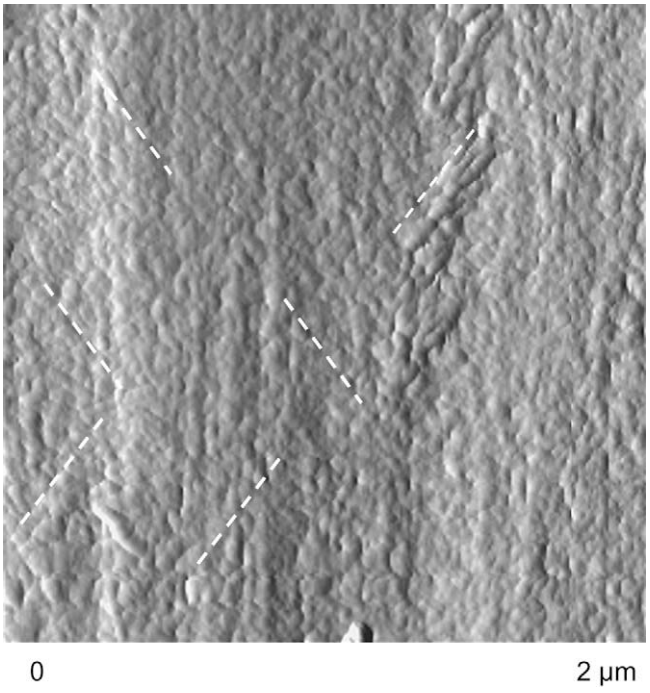

Fig. 8. Small scale AFM *error* image of PB-20 at the strain $\varepsilon = 150\%$.

of semi-crystalline polymers [16–19]. In the present case, this orientation scenario is consistent with the large scale oblique alignments of crystal fragments (Fig. 8). It suggests that, in spite of the small size of the lamella fragments at $\varepsilon = 150\%$, the material builds up neither the conventional fibrillar structure characterized by a meridian 2-point SAXS pattern [20,21] nor the chevron-like structure to which is associated a 4-point SAXS pattern with elongated lobes perpendicular to the draw direction [20,22–24]. This again is consistent with the AFM image of Fig. 8 indicating no trace of fibrillar structure.

The WAXS pattern at $\varepsilon = 150\%$ (Fig. 9b) discloses a strong equatorial reinforcement of the first two reflections assigned to the (110) and (300) planes of the hexagonal crystal lattice, while the third one associated with both the (220) and (211) planes is nearly isotropic. This crystalline texture indicates that the chain axis is almost parallel to the draw axis. Combining the WAXS and SAXS findings, and assuming that the chain stems were normal to the surface of the crystalline lamellae prior to deformation, one may conclude that the crystal fragments have actually undergone a plastic shear. The average shear strain of the crystal fragments at $\varepsilon = 150\%$ is $\gamma \approx \tan 50^\circ \approx 1.2$. Using the equivalence between shear and tensile strains [25],

$$H_{eq} = \gamma/\sqrt{3} \tag{2}$$

where $H_{eq} = \ln(1 + \varepsilon_{eq})$ is the equivalent Hencky strain and ε_{eq} the equivalent conventional tensile strain, it comes that $H_{eq} \approx 0.7$ for the crystal shear, otherwise $\varepsilon_{eq} \approx 100\%$ for the crystal component.

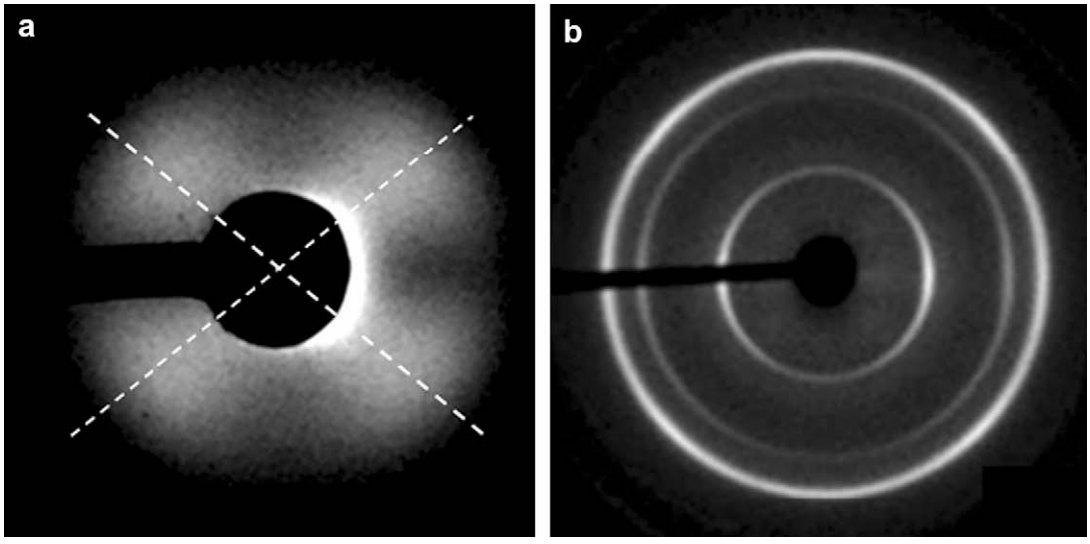

Fig. 9. SAXS (a) and WAXS (b) patterns of PB-20 for the strains $\varepsilon = 150\%$ (draw axis vertical).

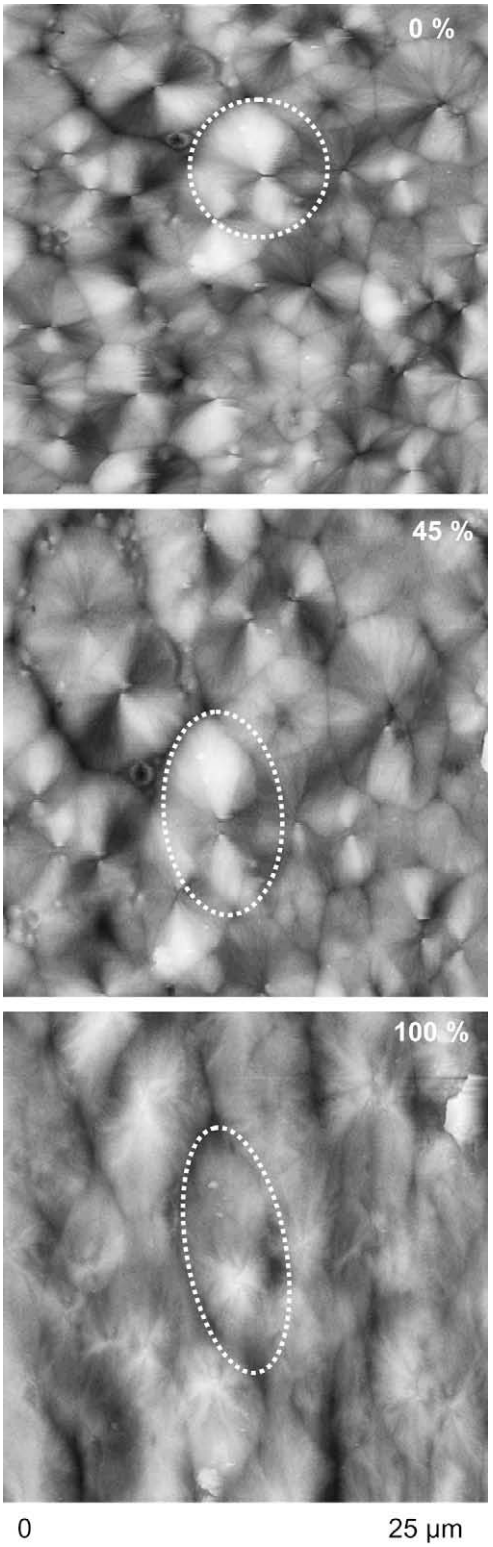

Fig. 10. Medium scale AFM *height* images (Z range = 4500 nm) of PB-5 for strains $\varepsilon = 0\%$, $\varepsilon = 45\%$ and $\varepsilon = 100\%$.

Finally, considering the crystal volume fraction of 45% in PB-20, the contribution of the crystal shear to the overall tensile strain is 45% at $\varepsilon = 150\%$. Therefore, homogeneous crystal shear that cannot be clearly observed on the AFM images of Figs. 5, 6 and 8 actually contributes about 1/3 to the total strain at $\varepsilon = 150\%$.

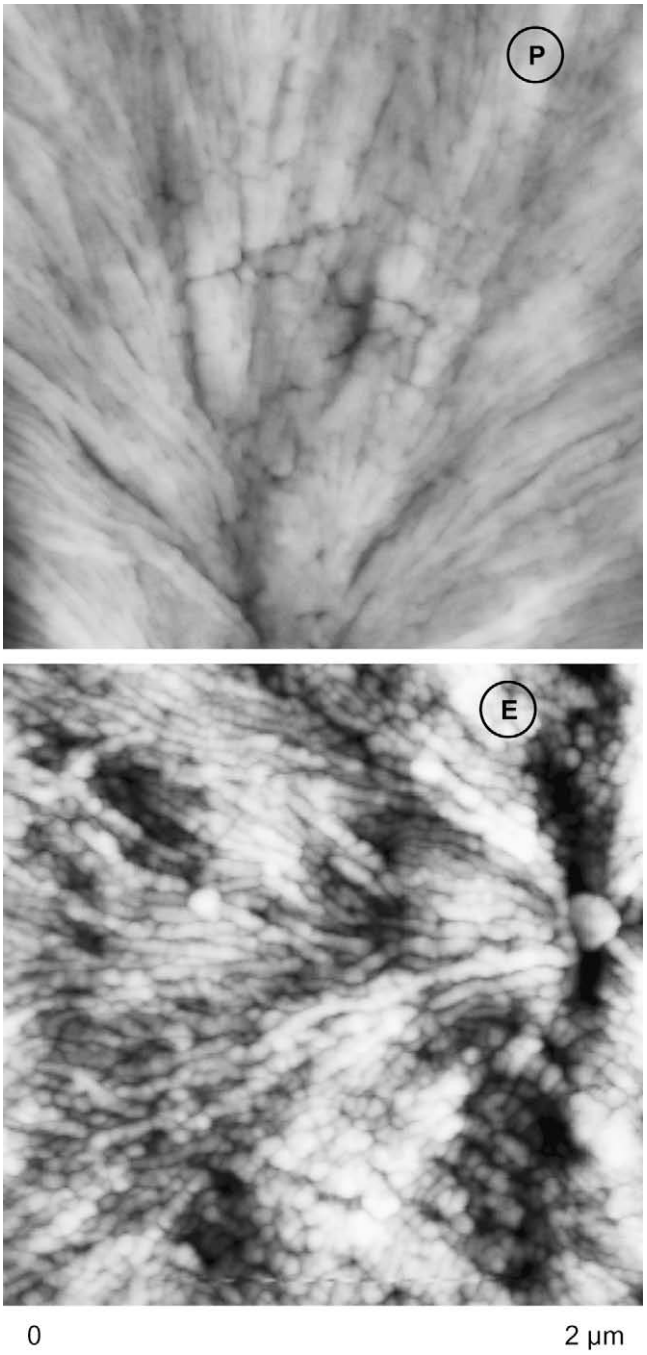

Fig. 11. Small scale AFM *height* images (Z range = 200 nm) in the polar (P) and equatorial regions (E) of a PB-5 spherulite for the strain $\varepsilon = 20\%$.

3.2. PB-5 films

Fig. 10 reports *height* images of PB-5 at strains $\varepsilon = 0\%$, $\varepsilon = 45\%$ and $\varepsilon = 100\%$. The small size of the spherulites makes local scale deformation more difficult to determine than in the case of PB-20. Notwithstanding, using the elliptical shape evolution of spherulites having well defined boundaries (Fig. 10) enables to assess local strains. It turns out that affinity between local and macroscopic strains is obeyed within the experimental accuracy, the relative departure being less than 15%. The homogeneity of the plastic deformation at the macroscopic scale (Fig. 2) doubtlessly results from a local scale homogeneous deformation. The deformation

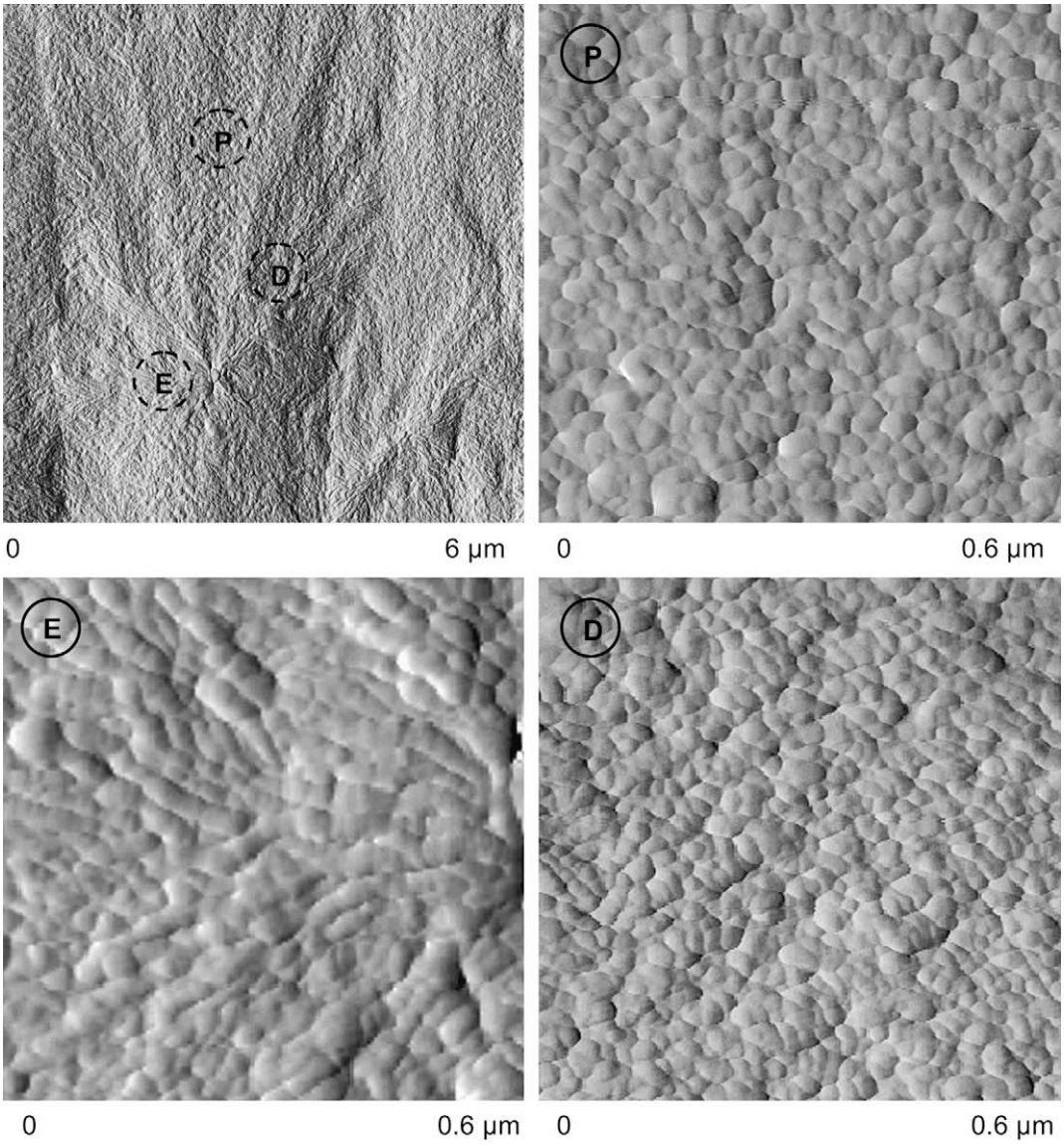

Fig. 12. Small scale AFM *error* images of PB-5 drawn at $\varepsilon = 100\%$ from the equatorial (E), polar (P) and diagonal (D) regions of the same spherulite.

affinity indeed requires an efficient stress transfer between adjacent spherulites that clearly appears in Fig. 10. The spherulites boundaries yet display a slight decrease of surface level with regard to the spherulite cores, as can be seen from their dark contrast, which means that the plastic deformation is not perfectly homogeneous over the whole spherulite volume. But as in the case of PB-20, there are absolutely no signs of inter-spherulitic cracks or crazes.

The small scale *height* images of Fig. 11 captured from PB-5 at the yield strain $\varepsilon \approx 20\%$ show that fragmentation is a predominant plastic process in all regions about the spherulite core, as in the case of PB-20. Again, the sporadic character of fragmentation suggests that it is a self-governed process.

The small scale *error* images of Fig. 12 recorded far beyond the yield point, i.e. at $\varepsilon \approx 100\%$, reveal that fragmentation proceeds further with increasing applied strain and gradually turns uniform over the whole spherulite surface. The lamella fragments have a rather narrow size distribution with an average size of about 20 nm. Besides, in spite of well defined spherulite boundaries, the 6 μm image of Fig. 12 clearly shows that the fragmentation process goes across the inter-spherulitic boundary without signs of hindrance from the structural heterogeneity. This reinforces the previous observation that neither cracks nor crazes develop at the spherulite boundaries and supports the assumption of an efficient stress transfer at the boundary.

4. Concluding discussion

The present study of the plastic deformation processes of polybutene having small size spherulites, namely PB-20 and the PB-5, is complementary to the previous study of polybutene having large spherulites, i.e. PB-200 [3]. It definitively shows that the structural factors in the size range between a few nanometers and several tens of microns have a tremendous incidence on the development of the plastic processes. As a matter of fact, large spherulites display intense crazing and cavitation leading to brittle behavior whereas small spherulites display homogeneous fragmentation, with very little cavitation if any, leading to large plastic deformation. This is strikingly contrasting with the plastic behavior of β-PP, for instance, which displays a high propensity for crazing irrespective of spherulite size in the range 20–200 μm [26–29].

A common point to small and large PB spherulites is yet the continuity of the plastic processes through the inter-spherulitic

boundaries. This contrasts with literature reports showing significant inter-spherulitic damage due to phase segregation of either amorphous species or immiscible additives. The present observations are relevant to high chemical homogeneity of the material and uniformity of local mechanical properties in both cases. This enables efficient stress transfer through the boundary in spite of the structural heterogeneity about the boundary. This conclusion is particularly relevant in the case of large spherulites which develop profuse crazing extending over several microns.

The presence or not of strain-induced cavities is of major concern regarding micromechanical modeling since homogeneous stress (or strain) distribution is a current assumption that may be not obeyed at a local scale. Pawlak and Galeski [30] have shown that depending on the level of crystal plastic compliance in comparison with the critical stress for cavitation, semi-crystalline polymers may generate cavitation or not upon tensile drawing. Nanoscopic cavities confined within the amorphous layers may eventually heal themselves upon unloading, as shown in the case of nylon6 [30,31]. In the present study, the stress drop during the time of relaxation and image recording does not exceed 15% of the applied stress, in the strain range beyond the yield point. Therefore, the non-observation of cavitation in either PB-20 or PB-5 is a piece of evidence that it actually did not occur since, if it had occurred, it would hardly have get healed. Another hint in favor of no cavitation is that the yield stress of PB-20 and PB-5 is about 3-fold lower than in the case of cavitation-prone PP and PA6 at RT, which means that cavitation would be much more energy-consuming than crystal slip, including localized slip. However, in the case of PB-200, the somewhat higher crystal thickness (Table 1) is likely to be responsible for a higher critical shear stress of the crystal (see Refs. [32–34] and the references cited therein) that may compare with the critical stress for interlamellar cavitation. The twice larger yield stress of PB-200 as compared with PB-20 (Fig. 2) supports this argument. This situation in PB-200 enables cavitation and subsequent profuse crazing [3].

Another direct consequence of the change in crystal lamella thickness is the change of the intercrystalline tie chain density [35], a structural factor often not taken into account because uneasy to assess. The lower crystal thickness of PB-20 should entail a significantly greater tie chain density than in PB-200. This structural factor is favorable for preventing cavitation of PB-20 at the border of the crystal fragments at the very moment of lamella fragmentation.

If the activation of uniform crystal slip could not be excluded in the present instance, it must be pointed out that it is of minor contribution to the global plastic strain in comparison with the fragmentation process and the subsequent rearrangement of crystal fragments. Previous work from the laboratory on nylon6 [8] and recent work on polylactone [36,37] revealed that early fragmentation of the crystalline lamellae is a rather common phenomenon in semi-crystalline polymers. This has been shown to result in mechanical damage as assessed from the gradual loss of stiffness with increasing plastic strain [37]. Work is in progress to account for these findings in a mechanical modeling based on a plasticity-damage coupling [38] without contribution from cavitation that did not appear to be a relevant factor in the present and above-mentioned investigations.

Last but not the least, fibrillar transformation is not a necessary pathway for large strain plastic deformation of semi-crystalline polymers.

To sum up, benefiting from the present and previous [3] studies on polybutene, a model polymer from the standpoint of structural sensitivity to processing conditions, it appears quite clear that theoretical approaches of the mechanical behavior cannot be applied in predictive purpose without checking that the modeling assumptions account for the actual deformation processes.

Acknowledgments

The authors are indebted to the European FEDER Program and the Région Nord/Pas-de-Calais (RNPdC) for funding to the Digital AFM equipment. The Centre National de la Recherche Scientifique and the RNPdC are also deeply acknowledged for the grant of a doctoral fellowship to C. Thomas.

References

[1] Seguela R. e-polymers; 2007, no 032, 1–20.
[2] Weynant E, Haudin J-M, G'Sell C. J Mater Sci 1980;15:2677–92.
[3] Thomas C, Ferreiro V, Coulon G, Seguela R. Polymer 2007;48:6041–8.
[4] Miller RL, Holland VF. J Polym Sci Polym Lett 1964;2:519–21.
[5] Kaszonyiova M, Rybnikar F, Geil PH. J Macromol Sci Phys 2005;B43:1095–114.
[6] Rubin ID. J Polym Sci Polym Lett 1964;2:747–9.
[7] (a) Ferreiro V, Pennec Y, Seguela R, Coulon G. Polymer 2000;41:1561–9;
(b) Ferreiro V, Coulon G. J Polym Sci Polym Phys 2004;42:687–701.
[8] Wunderlich B. Macromolecular physics. In: Crystal structure, morphology, defects, vol. 1. New York: Academic Press; 1973.
[9] Ward IM. Mechanical properties of solid polymers. New York: Wiley-Interscience; 1971.
[10] Staniek E, Seguela R, Escaig B, François. J Appl Polym Sci 1999;72:1241–7.
[11] Bowden PB, Young RJ. J Mater Sci 1974;9:2034–51.
[12] (a) Gaucher-Miri V, Seguela R. Macromolecules 1997;30:1158–67;
(b) Seguela R, Gaucher-Miri V, Elkoun S. J Mater Sci 1998;33:1273–9;
(c) Seguela R, Elkoun S, Gaucher-Miri V. J Mater Sci 1998;33:1801–17.
[13] Stribeck N. ACS Symp Ser 2000;739:41–56.
[14] Pakula T, Saijo K, Kawai H, Hashimoto T. Macromolecules 1985;18:1294–302.
[15] Meinel G, Morosoff N, Peterlin A. J Polym Sci Polym Phys 1970;8:1723–40.
[16] Hashimoto T, Fugimura M, Saijo K, Kawai H, Diamant J, Shen M. Adv Chem Ser 1979;176:257–75.
[17] Tarasov SG, Tsvankin D, Godovskii Ya, Yu K. Polym Sci USSR 1979;20:1728–36 (Engl. Transl. Vysokomolekulyarnye Soedineniya, Seriya A, 1978, 20, 1534-42.).
[18] Seguela R, Prud'homme J. Macromolecules 1981;14:197–202.
[19] Cohen Y, Albalak RJ, Dair BJ, Capel MS, Thomas EL. Macromolecules 2000;33:6502–16.
[20] Alexander LE. X-ray diffraction methods in polymer science. New York: Wiley Interscience; 1969.
[21] Galeski A. Prog Polym Sci 2003;28:1643–99.
[22] Gerasimov VI, Genin Ya, Tsvankin V, Ya D. J Polym Sci Polym Phys 1974;12:2035–46.
[23] Blöchl G, Owen A. J Colloid Polym Sci 1984;262:793–7.
[24] Song HH, Argon AS, Cohen RE. Macromolecules 1990;23:870–6.
[25] (a) Canova GR, Shrivastava S, Jonas JJ, G'Sell C. In: Newby JR, Niemeier BA, editors. Formability of metallic materials – 2000 A.D. Philadelphia: American Society for Testing and Materials; 1982;
(b) G'Sell C, Boni S, Shrivastava S. J Mater Sci 1983;18:903–18.
[26] Aboulfaraj M, G'Sell C, Ulrich B, Dahoun A. Polymer 1995;36:731–42.
[27] Grein C. Adv Polym Sci 2005;188:43–104.
[28] Krumova M, Henning S, Michler GH. Philos Mag 2006;86:1689–712.
[29] Henning S, Michler GH, Ania F, Balta-Calleja FJ. Colloid Polym Sci 2005;283:486–95.
[30] Pawlak A, Galeski A. Macromolecules 2005;38:9688–97.
[31] Galeski A, Argon AS, Cohen RE. Macromolecules 1988;21:2761–70.
[32] Darras O, Seguela R. J Polym Sci Polym Phys 1993;31:759–66.
[33] Seguela R. J Polym Sci Polym Phys 2002;40:593–601.
[34] Kazmierczak T, Galeski A, Argon AS. Polymer 2005;46:8926–36.
[35] Seguela R. J Polym Sci Polym Phys 2005;43:1729–48.
[36] Detrez F, Seguela R, Coulon G. 18ème Congrès Français de Mécanique; August 2007, Grenoble France (http://hdl.handle.net/2042/16131).
[37] Detrez F, Cantournet S, Seguela R, Coulon G. Materials science & technology conference MS&T'08, Pittsburgh, USA; October 2008.
[38] Detrez F, Cantournet S, Seguela R, in preparation.